
Three-Dimensional Characterization of Spherical Cryogenic Targets Using Ray-Trace Analysis of Multiple Shadowgraph Views

Introduction

In the laser-driven direct-drive approach to inertial confinement fusion (ICF), energy from many individual high-power lasers is delivered to a spherical target, causing a spherically symmetric implosion.¹ The 60-beam, 30-kJ OMEGA Laser System² is used to study direct-drive ignition (DDI), where the laser energy is deposited directly onto the target. For indirect-drive ignition (IDI), the laser energy is directed onto a metal container (a *hohlraum*) surrounding the target, creating x rays that deposit the energy onto the target.^{3,4} IDI is inherently less efficient than DDI but has less-restrictive symmetry requirements on the laser illumination.

Current designs for both DDI and IDI high-gain ICF targets require a layer of condensed hydrogen fuel that adheres to the inner surface of a spherical shell ablator. Photon energy delivered to the target ablates its outer surface, and the ablation pressure drives the fuel layer inward, compressing both it and the gaseous fuel at the target's center. The drive pressure is varied in time such that the fuel density is compressed by a factor of as much as 4000 while remaining relatively cold. Shock waves resulting from the drive-pressure history, along with compressive work, heat the gaseous-core "hot spot" to the high temperatures needed to initiate burning the fuel.

As the fuel layer is compressed and decelerates, perturbations on the inner ice surface act as amplitude seeds for the Rayleigh–Taylor instability^{5,6} on the inner surface. The nonlinear growth of this deceleration-phase instability mixes the cold compressed fuel layer with the hot-spot fuel vapor, reducing fusion yield or preventing ignition.^{7–10} Asymmetry-induced hydrodynamics can reduce the performance of ICF targets to well below that predicted by 1-D modeling.¹¹ Ignition requirements impose strong constraints on the illumination uniformity and on the sphericity of the target.¹²

The degrading effect of an inner-ice-surface perturbation on implosion performance depends on the perturbation's mode number, which is the ratio of the capsule's circumference to the wavelength of the perturbation. The surface roughness is charac-

terized in terms of a mode spectrum analogous to Fourier analysis. Since the target geometry is spherical, spherical harmonics $Y_{lm}(\theta, \varphi)$ form the basis functions used for the mode spectrum. Accurate surface characterization of ice layers requires reliable measurement of the layer's surface with submicron resolution at many points distributed over the surface of a target. Hydrodynamic codes then calculate capsule implosion performance using the measured surface mode power spectrum. The benchmarking of calculated target performance with experimental results is essential for designing ignition-scale targets and specifying their allowable surface roughness with confidence.

The DDI specifications¹² for the National Ignition Facility (NIF)¹³ require a total root-mean-square (rms) deviation of less than $1 \mu\text{m}$ for an ice layer with less than $0.25\text{-}\mu\text{m}$ rms from Fourier modes higher than $n = 10$. An ice-layer rms deviation of less than $1 \mu\text{m}$ is also required for successful IDI on the NIF.¹⁴ Measurement of the ice-layer radius over the entire surface with submicron resolution is required to verify success or failure at achieving the required specifications.

This article describes the optical backlit shadowgraphic 3-D characterization of cryogenic direct-drive-target ice layers at LLE using ray-trace analysis of the shadowgrams. The following sections (1) briefly describe the principles and equipment used to record a cryogenic-target shadowgram at LLE; (2) analyze the resolution of shadowgram measurements; (3) describe three-dimensional ice-layer reconstruction from multiple target views using the conventional assumption that the shadowgram bright ring can be directly related to the ice thickness based on spherically symmetric calculations; and (4) present a shadowgram analysis to which nonspherically symmetric ray tracing is added, thereby improving the 3-D ice-layer reconstruction by self-consistently calculating the effects of ice-layer asymmetries and roughness on the position of the bright ring in each view. The conclusions are presented in the final section.

Shadowgraphic Characterization of Ice Layers

Optical backlit shadowgraphy is the primary diagnostic used to measure ICF target ice-layer roughness.^{15–25} A shadow-

graph records the image of the light rays passing through a backlit target. The rays are reflected and refracted at the shell wall and ice-layer surfaces. Some rays are focused into characteristic rings. Ray-trace modeling of a typical cryogenic target using the *PEGASUS* code²⁶ has identified the specific reflections/refractions responsible for the brightest rings (see Fig. 109.44). The most-prominent ring or “bright ring” is the result of a single internal reflection off the inner solid/vapor interface of the ice layer. The position of the bright ring in the shadowgraph is directly correlated with the position of the inner surface of the ice layer and allows the nonuniformity of the inner surface to be characterized.

A high-magnification, high-fidelity backlit optical shadowgraphy system (see Fig. 109.45) is used to diagnose the ice-layer quality. A 627-nm red-light-emitting diode (LED) provides the backlighting. A 50- to 100- μ s pulse drives the LED to illuminate ($\sim f/5$) the target. Imaging optics ($\sim f/6$) magnify the target image on a DALSA charge-coupled-device (CCD) camera

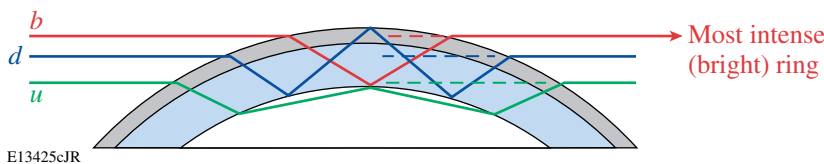


Figure 109.44 Ray-trace modeling of a cryogenic target has identified the sources of the most-intense rings. The bright ring (b) is by far the most intense.

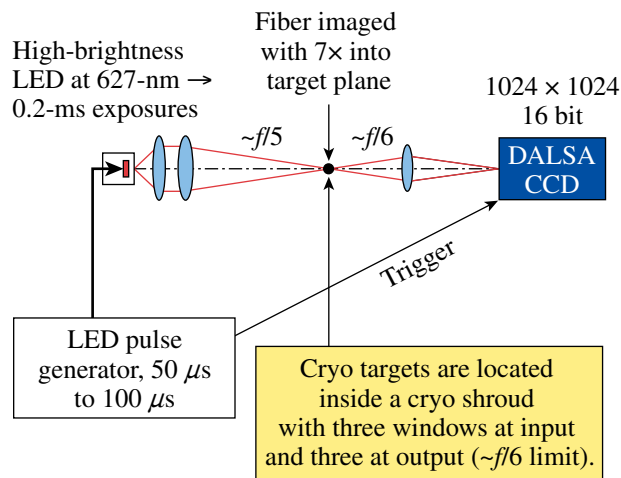


Figure 109.45 The LLE Cryogenic Target Characterization Stations are based on a diffuse $f/5$ source and $f/6$ imaging optics.

(12 bit, 1024 \times 1024) (Ref. 27) such that the camera typically images about 1.2 μ m per pixel. The camera is triggered by the same pulse that drives the LED.

A sample shadowgram of an LLE cryogenic D₂ target suspended from a beryllium “C-mount” by four threads of spider silk is shown in Fig. 109.46. The strong unbroken bright ring and mostly featureless central spot are indicative of the high quality of this ice layer. Two inner rings are also clearly visible.

Resolution of Shadowgram Rings

The analysis of the target image in an individual shadowgram consists of accurately determining the target center, unwrapping the image into polar coordinates, and measuring the radial positions of both the target edge and the bright ring’s peak intensity. Details of this procedure are published elsewhere.²¹ Here, the accuracy and resolution of these measurements are discussed.

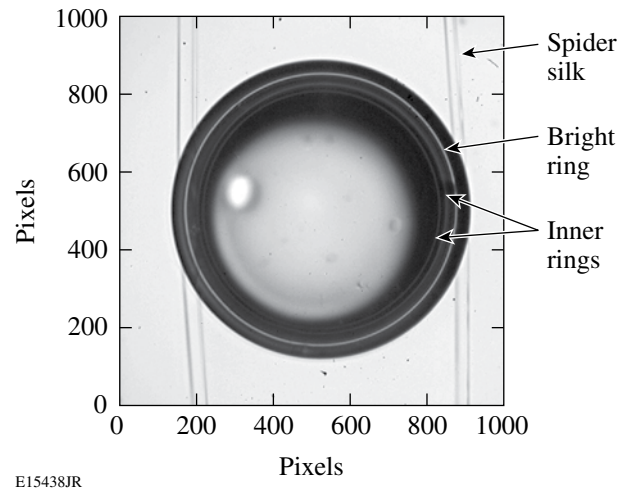


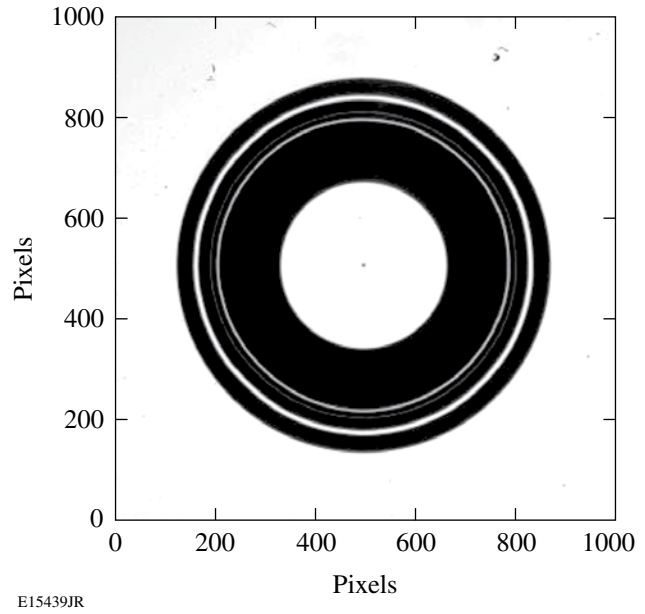
Figure 109.46 Shadowgram of a cryogenic target (876- μ m outer diameter, 4.2- μ m shell thickness, 79- μ m ice thickness) in a logarithmic scale. The fainter inner rings are clearly visible in the image. The bright-ring signal-to-noise ratio is typically over 20, and the effects of noise are reduced by the shadowgraph analysis routines.²¹ The offset of the light rays passing through the center of the target is due to an asymmetry in the spread of the illumination, which has little effect on the position of the bright ring.

Previously, by examining the bright-ring-measurement scatter for very smooth liquid hydrogen layers,²¹ the resolution of the measurements was estimated to be about 0.1 pixel (~0.12 μm). The high resolution of the bright-ring measurements has been verified using precision calibration targets as described here. The calibration targets are simulated target images of photolithographed chrome on glass.²⁸ A simulated image consists of a “perfectly” circular edge along with a bright ring (plus two fainter inner rings) with a known variation in radial position. The radial variation of the rings was calculated, using the linearized formula discussed in the next section, for an ice surface with a surface-deviation, Fourier-mode power spectrum of

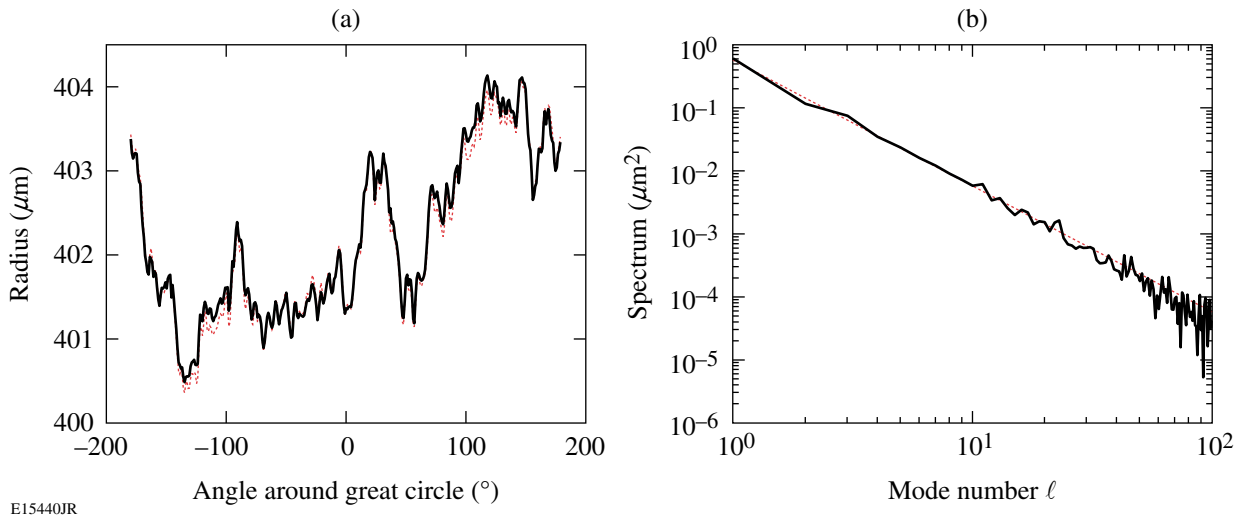
$$P_n = Cn^{-2} \tag{1}$$

for Fourier modes $n = 1$ to 100, where C was chosen such that the spectrum meets the DDI specification. The phase of each Fourier mode was randomized. This power spectrum and the calculated bright-ring position are shown in Fig. 109.47. The precision calibration target was photolithographed with a manufacturing tolerance of 0.1 μm. A shadowgram of this target taken in one of OMEGA’s Cryogenic Target Characterization Stations is shown in Fig. 109.48. This image has been analyzed using LLE’s standard shadowgram analysis routines, and the results are shown in Fig. 109.47. The measured bright-ring positions have a mean error of less than 0.1 μm (within the manufacturing tolerances of the calibration target), and the total rms error of the ring measurement is about 0.01 μm.

It is clear that the bright-ring position can be very accurately measured in the characterization station shadowgrams. The relationship of that ring position with the radius of the actual ice surface producing the ring is discussed in the next section.



E15439JR
Figure 109.48
Shadowgram of the photolithographed chrome-on-glass “dot-surrogate” target. The outer edge is a perfect circle to within the manufacturing tolerance (0.1 μm). The rings are simulated by uniform-thickness gaps in the dot. The inner rings are fainter than the bright ring because their gap width is less. The radial positions of the rings vary around the target and are calculated for an ice surface whose roughness meets the DDI requirements.



E15440JR
Figure 109.47
The measured (solid) bright ring for the simulated dot-surrogate target is an excellent match to the design specification (dotted) in terms of both (a) radial position and (b) power spectrum.

Three-Dimensional Ice-Layer Reconstruction Using Multiple Shadowgraph Views

An important feature of LLE's Cryogenic Target Shadowgraphy System is the use of multiple views of the target to fully characterize the ice surface. Multiple views allow a far-more-complete surface characterization than is possible from a single view. Even with three mutually orthogonal views, it can be shown that there is only a small chance of detecting many local ice defects.²⁹

In the LLE Cryogenic Target Characterization Stations, the targets are rotated to provide a large number of different views for a single camera. The maximum number of views is limited only by the step size of the rotation stepper motor, which is a few tenths of a degree. Shadowgrams are typically recorded at 15° intervals, producing a total of 48 independent views between two cameras in each characterization station. The two cameras have approximately orthogonal views: one camera views the target center from an angle of 26.56° above the equator and the second camera, located 109.96° azimuthally from the first, views the target center from 12.72° above the equator. These view angles are determined by the location of the layering sphere windows that are aligned with the OMEGA target chamber's viewing ports, which are used to center the target at shot time. These views are not optimum for target characterization. An off-the-equator viewing angle always results in unviewable regions surrounding the rotation poles; these unviewable "polar caps" are apparent in Fig. 109.49(a).

The standard method of shadowgram analysis assumes that the ice surface position along a great circle perpendicular to

the shadowgraph view can be uniquely determined from the observed bright-ring position for that view^{17,22–25} by characterizing the ice-to-bright-ring relationship using a ray-trace study of spherically symmetric targets with varying ice thickness. At LLE, ray-trace modeling of a typical cryogenic target using the PEGASUS code²⁶ has identified how the shadowgram ring positions vary with the target parameters such as the shell outer radius and thickness, the D₂-ice thickness, the shell index of refraction, and the D₂ index of refraction. The PEGASUS code is two dimensional and assumes spherical symmetry in the target. A linearized formula derived from this modeling is used to determine the inner-ice-surface radius from the position of the bright ring for given target parameters.

A 3-D representation of the ice layer can be constructed from the ice-surface positions determined from the multiple shadowgram views. Figure 109.49 shows a target's inner ice surface reconstructed from a target rotation of 24 separate views. The surface is dominated by low-mode-number asymmetries, but very different Fourier modes are observed for any given great circle. For this data set, the ice-surface 1-D rms roughness of the individual great-circle observations varies from 2.6 μm to 5.3 μm with an average value of 3.5 μm. This particular data set was selected for the following reasons:

- The outer surface is very smooth and symmetric and should have little effect on the bright ring.
- The optical distortion from collection optics was well minimized for these images.
- The bright ring is smooth and has few breaks.

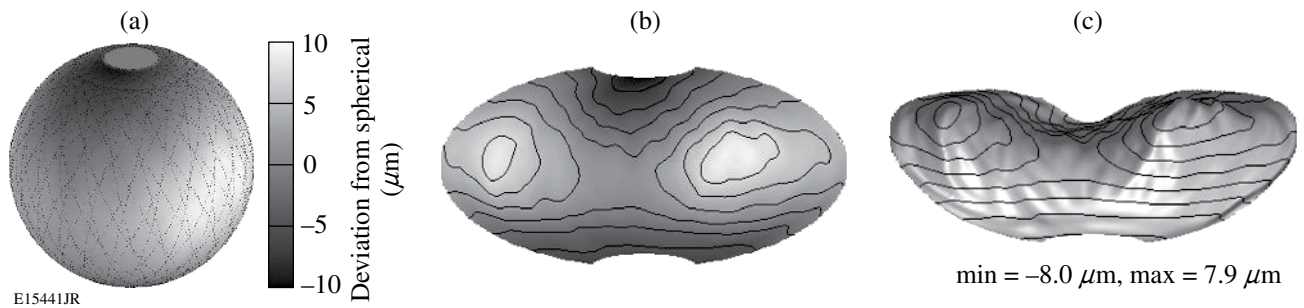


Figure 109.49 Three-dimensional representation of a cryogenic inner ice surface (μm) displayed (a) on a spherical surface, (b) using the Aitoff projection with contour lines, and (c) using the Aitoff projection with surface elevation. These displays are constructed by interpolating all the individual data from the many great-circle observations to an evenly spaced (θ, φ) surface grid. The dotted lines in (a) show the location of the actual great circles observed in the individual shadowgraphs. The "polar caps" crossed by none of the great-circle observations are clearly visible.

As mentioned earlier, computer modeling of a spherical implosion, including instability growth, requires an ice-roughness spectrum described in terms of spherical-harmonics-basis functions $Y_{\ell m}(\theta, \phi)$ on the ice surface:

$$R(\theta, \phi) = \sum_{\ell=0}^{\infty} \sum_{m=-\ell}^{\ell} A_{\ell m} Y_{\ell m}(\theta, \phi) \quad (\mu\text{m}). \quad (2)$$

This description gives a Legendre-mode power spectrum and total surface variance of

$$P_{\ell} = \frac{1}{4\pi} \sum_{m=-\ell}^{\ell} |A_{\ell m}|^2 \quad (\mu\text{m}), \quad (3)$$

$$\sigma_{\text{rms}}^2 = \sum_{\ell=1}^{\infty} P_{\ell} \quad (\mu\text{m}^2), \quad (4)$$

respectively. The P_{ℓ} spectrum represents an average over all azimuthal modes.

The P_{ℓ} spectrum for high mode numbers can be inferred from the Fourier power spectra of the many great circles observed. If one assumes that the surface perturbations are randomly distributed, the great-circle 1-D Fourier-mode power spectrum, averaged over many great circles, can be mapped³⁰ to an equivalent Legendre-mode power spectrum. The assumption of randomly distributed perturbations limits the applicability of the mapping to higher mode numbers. At LLE the ice-surface positions are directly fit to spherical harmonics to determine the lower mode numbers (up to some ℓ_{max}).²¹

The results of a direct $Y_{\ell m}(\theta, \phi)$ fit are shown in Figs. 109.50 and 109.51 for a fit up to $\ell_{\text{max}} = 10$. The surface reconstruction in Fig. 109.51 based on the low-mode-number fit is a good match to the data shown in Fig. 109.49. The Legendre power spectrum P_{ℓ} corresponding to this fit along with the higher mode numbers determined by the mapping method is displayed in Fig. 109.50. Target reconstructions using the standard analysis have successfully detected low-mode asymmetries in the ice layer, allowing the identification and correction of the sources of the layering sphere temperature isotherm asymmetries that cause them.³¹

The maximum mode number fit, ℓ_{max} , is limited by the largest space between sampled points on the surface. For typical LLE targets, the largest gap in the surface data occurs at the unviewable polar cap of the target. The maximum mode number that can be reliably fit is also reduced by the many smaller surface gaps between great-circle measurements, noise in the data, uneven surface weighting (sections crossed by several great circles are more heavily weighted), and the fact that the data do not agree

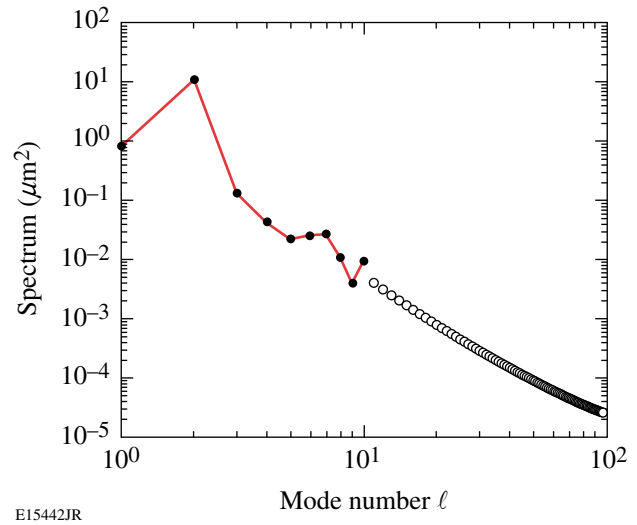


Figure 109.50

Legendre-mode power spectrum P_{ℓ} of the ice surface. The dots correspond to the low-mode-number (up to $\ell_{\text{max}} = 10$) direct fit. The circles result from mapping the average Fourier-mode spectrum of the many great circles.

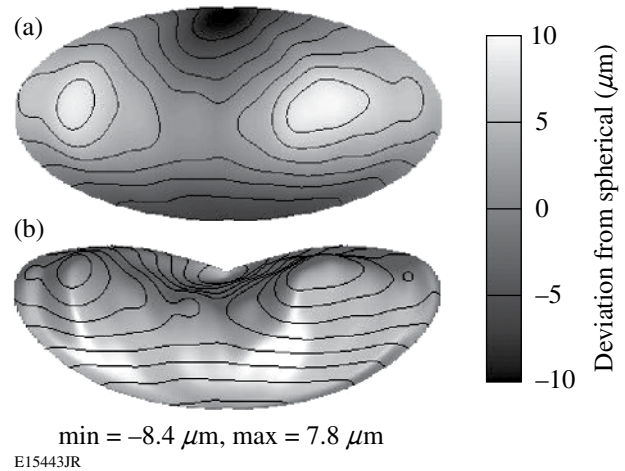
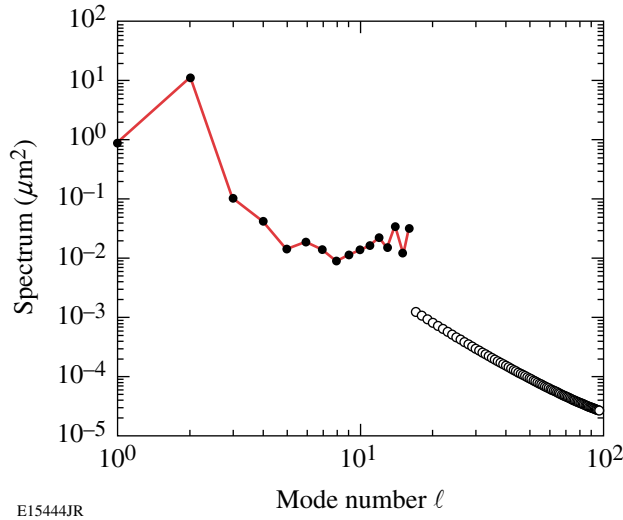


Figure 109.51

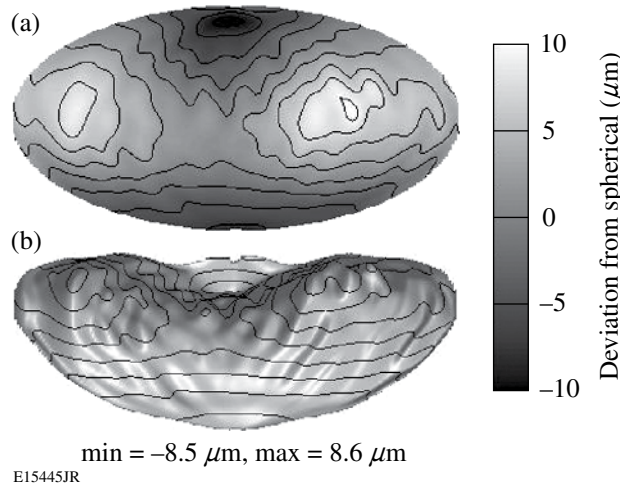
Three-dimensional reconstruction of a cryogenic inner ice surface (μm) based on a direct $Y_{\ell m}(\theta, \phi)$ fit to the measured data (up to $\ell_{\text{max}} = 10$) (a) using the Aitoff projection with contour lines and (b) using the Aitoff projection with surface elevation. A comparison with Fig. 109.49 shows that the low-mode features are well matched by the fit. Although the actual great-circle data are used in the fitting, the results are mapped to an evenly spaced (θ, ϕ) surface grid using the $Y_{\ell m}$ coefficients for better display.

at “cross-over” points (see the next section). The sum of these effects typically limits the direct surface fit to mode numbers up to about $\ell_{\text{max}} = 10$. The exact limit varies with each data set. The results of fitting too high an ℓ_{max} are shown in Figs. 109.52 and 109.53, where the fit has been extended to $\ell_{\text{max}} = 16$. The power spectrum in Fig. 109.52 is rising as mode numbers approach

ℓ_{\max} , a trend not observed in the Fourier analysis of the bright rings. The combination of a too high ℓ_{\max} along with the spaces between data circles and data mismatch at the great-circle cross-over points produces a fit with more structure than seen in the individual bright rings. This increased structure and “crinkling” are evident in Fig. 109.53.



E15444JR
Figure 109.52
Legendre-mode power spectrum P_ℓ of the ice surface. The dots correspond to the low-mode-number (up to $\ell_{\max} = 16$) direct fit. The circles result from mapping the average Fourier-mode spectrum of the many great circles.

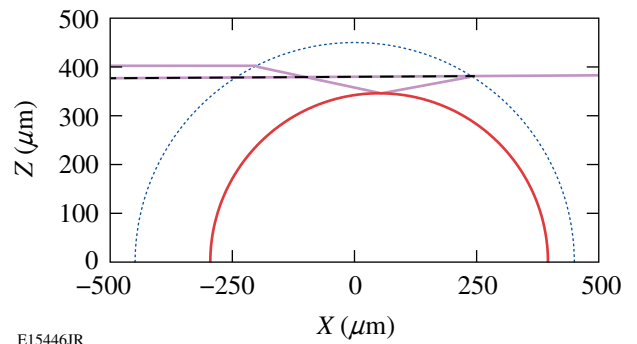


E15445JR
Figure 109.53
Three-dimensional reconstruction of a cryogenic inner ice surface (μm) based on a direct $Y_{\ell m}(\theta, \phi)$ fit to the measured data (up to $\ell_{\max} = 16$) (a) using the Aitoff projection with contour lines and (b) using the Aitoff projection with surface elevation. A comparison with Fig. 109.49 shows a large amount of mid-mode noise in the fit.

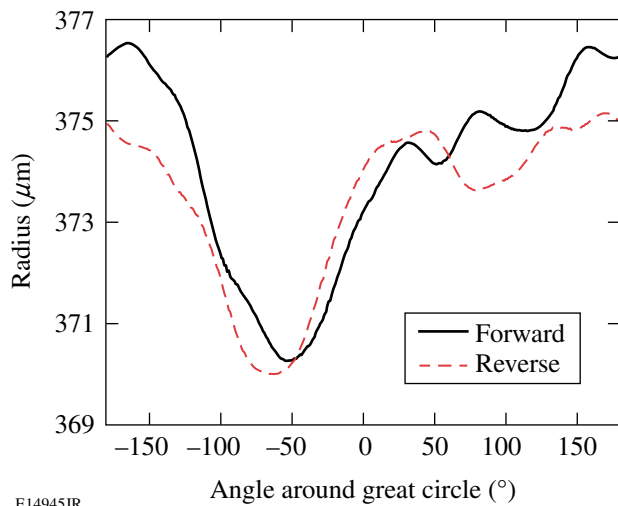
Ray-Trace Analysis

Despite the success of the standard analysis, it is well known^{18–20,24} that the assumption that the ice-surface position along a great circle perpendicular to the shadowgraph view can be directly correlated to the observed bright-ring position for that view is valid only for perfectly spherical symmetry. Koziowski *et al.*¹⁸ showed that a shift in the ice layer along the viewing axis will alter the bright-ring position and “significantly shift the apparent ice-layer thickness.” This effect can be easily seen in Fig. 109.54, which shows the ray path of the bright ring for a target layer shifted along the viewing axis. For imperfect ice layers, Koch *et al.*^{19,20} note that “correlation depends on the height and curvature of the imperfection.” To illustrate this, the bright-ring radii predicted by 3-D ray tracing of a simulated ice surface constructed from spherical harmonics for opposing views are shown in Fig. 109.55. The predicted bright rings show general similarities in the low-mode structures but differ greatly in the higher-mode detail. This explains why the ice surfaces determined by the standard method do not agree at the cross-over points of the views.

If the shadowgrams were viewed along the equator and exactly opposing views could be measured, the average position of two bright rings would show a good correlation to the ice-surface position along the great circle perpendicular to the views.³² In this case the standard method can accurately be applied to the averaged bright ring. If one has nonequatorial views, exactly opposing views cannot be recorded. A study of two above-the-equator views in the Cryogenic Target Characterization Stations for OMEGA rotated 180° about the polar



E15446JR
Figure 109.54
The ray path that produces the bright ring in a target where the ice surface is shifted along the line of view shows how asymmetries affect the bright ring. When viewed from the right, the bright ring appears lower than when viewed from the left. The standard analysis would determine a quite-different ice thickness for each view. For an unshifted layer, the rays on both sides would be at the same height and the bright ring would appear the same for both views.



E14945JR

Figure 109.55

Bright-ring radii predicted by 3-D ray tracing of an asymmetric ice surface for opposing views show very different structures. The standard method of shadowgram analysis assumes that both views will be identical and will depend solely on the ice radius at the great circle perpendicular to the view. In fact, the bright-ring radii also depend on the angle of the ice surface relative to each view, and the bright ring may not be centered on rays that strike the ice surface at the great circle.

axis showed that only the lowest modes can be determined with any accuracy by averaging two bright rings.³³

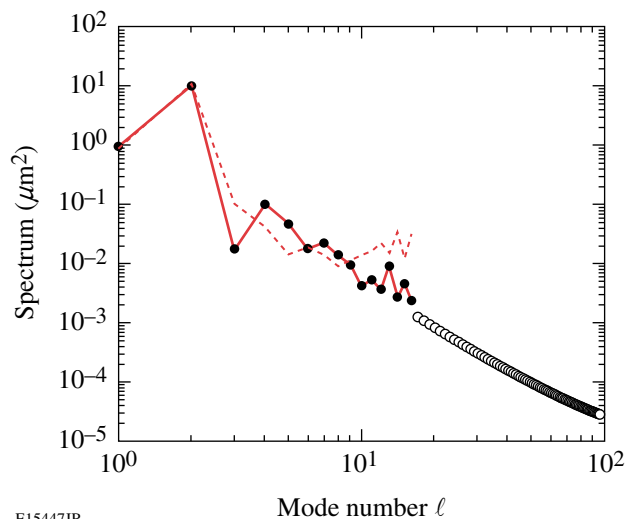
To self-consistently and accurately determine the 3-D ice surface from shadowgram bright-ring measurements requires the modeling of the effect that the ice-surface asymmetries and defects have on the bright-ring position and including this modeling into the shadowgram analysis. Koziowski *et al.*¹⁸ accomplished this in a limited fashion by using interferometry to measure the P1 ice-layer mode along the viewing axis, then correcting the bright-ring position for the effect of the P1 based on a ray-trace study. The ray-trace shadowgram analysis at LLE uses 3-D ray tracing to simultaneously fit the bright-ring measurements for all views (typically 48 different views) to a multimode (up to $\ell = 18$) spherical-harmonic representation of the ice layer.

Producing a simulated full shadowgram for a nonspherically symmetric ice layer can take days of CPU time^{20,24} due to the large number of ray-trace calculations required. For this fitting analysis, where many iterations of varying a large number of spherical-harmonic components is required, an alternative was found based on the observation that for spherically symmetric targets, the peak intensity of the bright ring is centered on rays whose paths on both sides of the target are along the viewing axis. This is a poor approximation for asymmetric layers such as a melted layer that is very offset from the view angle, but it

is a good approximation for the quasi-symmetrical case of a typical well-layered OMEGA cryogenic target.

With the above assumption, one need only follow one ray for each measured bright-ring position used in the fitting. The rays are launched backward from the measured bright-ring positions along their viewing angles and followed through the target and out the other side where the divergences of the rays' final paths from the view angles are recorded. Nonlinear fitting iterations are employed to adjust the spherical-harmonic description of the ice surface, minimizing the divergence of all the rays from the viewing angles. Typical total fitting times are of the order of several hours to a day, depending on the number of measurements (typically 180 points from each of 48 views) and the number of spherical-harmonic components fit, which varies as $(\ell_{\max} + 1)^2$. The nonlinear fitting routine constrains the maximum peak-to-valley variation of the ice surface to be similar to the maximum variation in the bright-ring position, preventing large peak-to-valley structures from occurring on the surface between the data rings or in the polar cap.

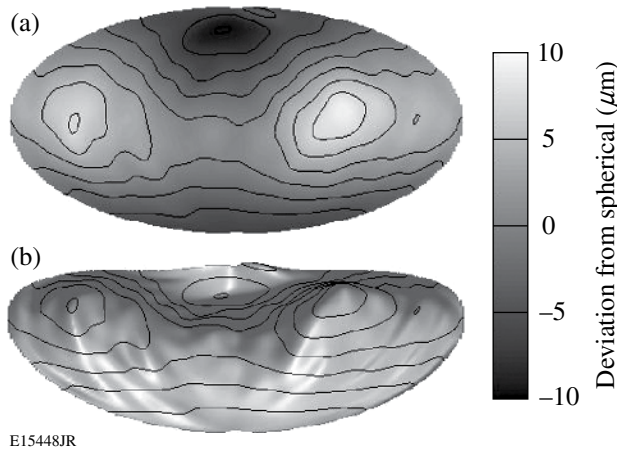
An example of the results from the ray-trace analysis with $\ell_{\max} = 16$ is shown in Figs. 109.56–109.58. The ice-surface Legendre-mode power spectrum is well behaved up to this ℓ_{\max} (Fig. 109.56), and the surface reconstructs show less anomalous structure (Fig. 109.57) than the standard method.



E15447JR

Figure 109.56

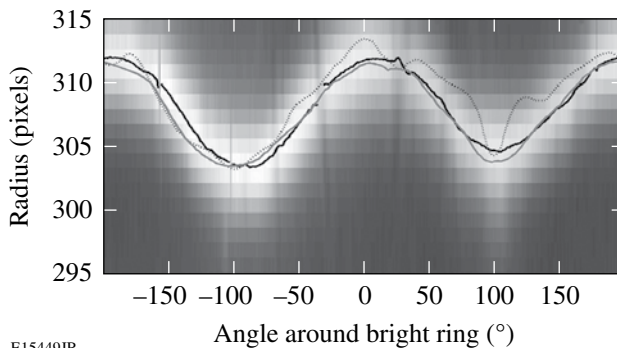
Legendre-mode power spectrum P_ℓ of the ice surface. The solid dots correspond to the low-mode-number (up to $\ell_{\max} = 16$) ray-trace fit while the dashed line redisplay the standard method fit (up to $\ell_{\max} = 16$). The ray-trace analysis is well behaved up to higher mode numbers than the standard method. The circles are the result from mapping the average Fourier-mode spectrum of the many great circles to determine the higher Legendre modes.



E15448JR

Figure 109.57

Three-dimensional reconstruction of a cryogenic inner ice surface (μm) based on a ray trace $Y_{lm}(\theta, \phi)$ fit to the measured data (up to $\ell_{\text{max}} = 16$) (a) using the Aitoff projection with contour lines and (b) using the Aitoff projection with surface elevation. This ray-trace fit shows less-artificial structure than the standard fit of Fig. 109.53.



E15449JR

Figure 109.58

Unwrapping of a sample bright ring in polar coordinates shows that the measured bright-ring positions (black line) are much better matched by the predicted bright-ring positions using the ray-trace analysis ice surface (gray line) than by the bright ring predicted using the ice surface determined by the standard method (dotted line).

Figure 109.58 shows a measured bright ring taken from one of the 48 different views of a D_2 -ice layer in an OMEGA cryogenic target. The ice surface determined using the standard method with $\ell_{\text{max}} = 16$ (Fig. 109.53) would produce the bright ring shown by the dotted line according to ray-trace calculations using that surface. The standard deviation between the measured bright rings for the 48 different views and their standard method predictions is $1.5 \mu\text{m}$.

The ice surface determined by the ray-trace analysis (Fig. 109.57) gives the bright-ring prediction shown by the solid gray line in Fig. 109.58. This surface produces a much

better match to the observed bright ring. The standard deviation between the measured bright rings for the 48 different views and their ray-trace analysis predictions is $0.8 \mu\text{m}$, a reduction of 45% from the standard method.

Summary and Discussion

It has been shown that the bright-ring position can be measured very precisely, but accurately correlating the bright-ring position to an ice-surface position is difficult. The standard method of applying spherically symmetric bright-ring calculations is inaccurate for asymmetric ice layers. Incorporating asymmetric ray tracing directly into the bright-ring analysis allows a self-consistent fitting of the bright rings from multiple views to an ice surface. Ray-tracing analysis reduced the error between the measured bright rings (for 48 different views) and those predicted for the fitted ice surface by 45% in comparison with the ice surface determined by the standard analysis.

It may be possible to further improve the performance of the ray-trace shadowgram analysis by

- modeling the bright-ring position, directly taking into account the uncollimated illumination of the actual shadowgraphy instead of assuming that the ring is centered on rays parallel to the viewing angles,
- fitting the optical differences between the views (magnification, focal position, etc.),
- adding some localized (e.g., spherical wavelet) defects to the ice-surface fitting to account for bright-ring features too localized to be fit by spherical harmonics and a reasonable ℓ_{max} , and
- including the effects of outer-surface perturbations on the bright ring that are believed to be responsible for some sharp features in the bright ring.

It is important to note that as the ice-layer quality improves and becomes more symmetric, the accuracy of the standard method improves. Initial studies of DT cryogenic targets for OMEGA³⁴ indicate that beta-layered DT targets are very smooth and symmetric and good candidates for accurate standard analyses. These very symmetric layers may still benefit from ray-trace analysis by isolating the effects of outer-surface perturbations on the bright ring that can be even larger than the actual ice-surface effects.

LLE is building a cryogenic fill-tube target station that will allow validation of this ray-trace modeling and shadowgram

analysis. The station will possess target rotation capabilities and equatorial views for both shadowgraphy and x-ray phase-contrast³⁵ layer diagnostics, allowing a direct comparison of ray-trace shadowgraphic analysis with (1) the standard analysis; (2) the standard analysis using averaged bright rings from opposing views; and (3) x-ray-phase-contrast direct measurements of the ice surface.

ACKNOWLEDGMENT

This work was supported by the U.S. Department of Energy Office of Inertial Confinement Fusion under Cooperative Agreement No. DE-FC52-92SF19460, the University of Rochester, and the New York State Energy Research and Development Authority. The support of DOE does not constitute an endorsement by DOE of the views expressed in this article.

REFERENCES

1. J. Nuckolls *et al.*, *Nature* **239**, 139 (1972).
2. T. R. Boehly, D. L. Brown, R. S. Craxton, R. L. Keck, J. P. Knauer, J. H. Kelly, T. J. Kessler, S. A. Kumpan, S. J. Loucks, S. A. Letzring, F. J. Marshall, R. L. McCrory, S. F. B. Morse, W. Seka, J. M. Soures, and C. P. Verdon, *Opt. Commun.* **133**, 495 (1997).
3. J. D. Lindl, *Phys. Plasmas* **2**, 3933 (1995).
4. J. D. Lindl, *Inertial Confinement Fusion: The Quest for Ignition and Energy Gain Using Indirect Drive* (Springer-Verlag, New York, 1998), Chap. 6, p. 61.
5. Lord Rayleigh, *Proc. London Math Soc.* **XIV**, 170 (1883).
6. G. Taylor, *Proc. R. Soc. London Ser. A* **201**, 192 (1950).
7. V. Lobatchev and R. Betti, *Phys. Rev. Lett.* **85**, 4522 (2000).
8. M. C. Herrmann, M. Tabak, and J. D. Lindl, *Phys. Plasmas* **8**, 2296 (2001).
9. R. Betti, K. Anderson, V. N. Goncharov, R. L. McCrory, D. D. Meyerhofer, S. Skupsky, and R. P. J. Town, *Phys. Plasmas* **9**, 2277 (2002).
10. R. P. J. Town and A. R. Bell, *Phys. Rev. Lett.* **67**, 1863 (1991).
11. D. D. Meyerhofer, J. A. Delettrez, R. Epstein, V. Yu. Glebov, V. N. Goncharov, R. L. Keck, R. L. McCrory, P. W. McKenty, F. J. Marshall, P. B. Radha, S. P. Regan, S. Roberts, W. Seka, S. Skupsky, V. A. Smalyuk, C. Sorce, C. Stoeckl, J. M. Soures, R. P. J. Town, B. Yaakobi, J. D. Zuegel, J. Frenje, C. K. Li, R. D. Petrasso, D. G. Hicks, F. H. Séguin, K. Fletcher, S. Padalino, C. Freeman, N. Izumi, R. Lerche, T. W. Phillips, and T. C. Sangster, *Phys. Plasmas* **8**, 2251 (2001).
12. P. W. McKenty, V. N. Goncharov, R. P. J. Town, S. Skupsky, R. Betti, and R. L. McCrory, *Phys. Plasmas* **8**, 2315 (2001).
13. W. J. Hogan, E. I. Moses, B. E. Warner, M. S. Sorem, and J. M. Soures, *Nucl. Fusion* **41**, 567 (2001).
14. S. W. Haan *et al.*, *Fusion Sci. Technol.* **49**, 553 (2006).
15. J. K. Hoffer *et al.*, *Fusion Technol.* **30**, 529 (1996).
16. J. D. Sheliak *et al.*, *Fusion Technol.* **30**, 83 (1996).
17. D. N. Bittner *et al.*, *Fusion Technol.* **35**, 244 (1999).
18. B. J. Koziowski *et al.*, in *Inertial Fusion Sciences and Applications 2003*, edited by B. A. Hammel, D. D. Meyerhofer, J. Meyer-ter-Vehn, and H. Azechi (American Nuclear Society, La Grange Park, IL, 2004), pp. 762–765.
19. J. A. Koch *et al.*, *Fusion Technol.* **38**, 123 (2000).
20. J. A. Koch *et al.*, *Fusion Sci. Technol.* **43**, 55 (2003).
21. D. H. Edgell, W. Seka, R. S. Craxton, L. M. Elasky, D. R. Harding, R. L. Keck, and M. D. Wittman, *Fusion Sci. Technol.* **49**, 616 (2006).
22. I. V. Aleksandrova *et al.*, *J. Phys. D: Appl. Phys.* **37**, 1163 (2004).
23. E. R. Koresheva *et al.*, *Nucl. Fusion* **46**, 890 (2006).
24. F. Lamy *et al.*, *Fusion Sci. Technol.* **48**, 1307 (2005).
25. F. Gillot *et al.*, *Fusion Sci. Technol.* **49**, 626 (2006).
26. S. Jin, *2002 Summer Research Program for High School Juniors at the University of Rochester's Laboratory for Laser Energetics*, Rochester, NY, LLE Report No. 329, LLE Document No. DOE/SF/19460-479 (2003).
27. DALSA, Waterloo, Ontario, Canada, N2V 2E9 (<http://www.dalsa.com>).
28. APPLIED IMAGE, Inc., Rochester, NY 14609, (<http://www.applied-imagegroup.biz>).
29. R. B. Stephens *et al.*, *Fusion Sci. Technol.* **45**, 210 (2004).
30. S. Pollaine and S. Hatchett, *Nucl. Fusion* **44**, 117 (2004).
31. D. R. Harding, D. D. Meyerhofer, S. J. Loucks, L. D. Lund, R. Janezic, L. M. Elasky, T. H. Hinterman, D. H. Edgell, W. Seka, M. D. Wittman, R. Q. Gram, D. Jacobs-Perkins, R. Early, T. Duffy, and M. J. Bonino, *Phys. Plasmas* **13**, 056316 (2006).
32. G. Balonek, *2004 Summer Research Program for High School Juniors at the University of Rochester's Laboratory for Laser Energetics*, University of Rochester, Rochester, NY, LLE Report No. 337, LLE Document No. DOE/SF/19460-590 (2005).
33. R. Wu, *2005 Summer Research Program for High School Juniors at the University of Rochester's Laboratory for Laser Energetics*, University of Rochester, Rochester, NY, LLE Report No. 343 (2006).
34. T. C. Sangster, R. Betti, R. S. Craxton, J. A. Delettrez, D. H. Edgell, L. M. Elasky, V. Yu. Glebov, V. N. Goncharov, D. R. Harding, D. Jacobs-Perkins, R. Janezic, R. L. Keck, J. P. Knauer, S. J. Loucks, L. D. Lund, F. J. Marshall, R. L. McCrory, P. W. McKenty, D. D. Meyerhofer, P. B. Radha, S. P. Regan, W. Seka, W. T. Shmayda, S. Skupsky, V. A. Smalyuk, J. M. Soures, C. Stoeckl, B. Yaakobi, J. A. Frenje, C. K. Li, R. D. Petrasso, F. H. Séguin, J. D. Moody, J. A. Atherton, B. D. MacGowan, J. D. Kilkenny, T. P. Bernat, and D. S. Montgomery, "Cryogenic DT and D₂ Targets for Inertial Confinement Fusion," to be published in *Physics of Plasmas* (invited).
35. D. S. Montgomery, A. Nobile, and P. J. Walsh, *Rev. Sci. Instrum.* **75**, 3986 (2004).